
USING GRIDPOINT RELAXATION FOR FORECAST ERROR DIAGNOSTICS IN NEURAL WEATHER MODELS

Uroš Perkan¹ and **Žiga Zaplotnik^{2,1}**

¹University of Ljubljana, Faculty of Mathematics and Physics,
Jadranska 19, 1000 Ljubljana, Slovenia

²European Centre for Medium-range Weather Forecasts,
Robert-Schuman-Platz 3, 53175 Bonn, Germany

ABSTRACT

Notable advantages of deep-learning (DL) weather prediction models over traditional physics-based models are their auto-differentiability and low computational cost. This allows extensive diagnostics of the origins of the forecast errors. We use our convolutional encoder-decoder model, ConvCastNet, to systematically nudge subdomains of the forecast fields towards a "true" weather state (analysis) and monitor the forecast skill improvements in other subdomains. Our results show that an 8-day mid-latitude weather forecast improves substantially with relaxation in the stratosphere and the boundary layer, whereas relaxation in the tropics has no significant impact. This highlights the importance of accurately representing the stratosphere and the planetary boundary layer for medium-range weather prediction and the limited impact of tropical variability on mid-latitudes forecasts. Additionally, we investigate the relationship between model error sensitivity to initial conditions and relaxation experiments. By utilising the model's auto-differentiability, we analyse saliency maps, i.e. the gradients of the forecast errors with respect to input fields, to identify overlapping regions of large error sensitivity and high impact of relaxation to truth. We believe that this combined approach provides valuable heuristics for diagnosing neural model errors and guiding targeted model improvements.

1 Introduction

Extensive research has established data-driven deep-learning (DL) weather prediction models as fast, energy-efficient, and skilful tools for short- and medium-range weather prediction. Some of the most prominent architectures include convolutional neural networks (CNN) [Weyn et al., 2019, 2020, 2021], graph neural networks [Keisler, 2022, Lam et al., 2023, Lang et al., 2024], transformers [Nguyen et al., 2023, Bi et al., 2023, Chen et al., 2023, Bodnar et al., 2024], Fourier neural operators [Bonev et al., 2023] and hybrids [Pathak et al., 2022, Price et al., 2024]. Regional DL models have also outperformed physics-based models according to some standard metrics [Andrychowicz et al., 2023]. Even though data-driven DL models have been shown to be superior to physics-based models in some aspects, they are distinct from their physics-based counterparts in their lower prior physical knowledge and weaker inductive biases, making them susceptible to predicting non-realistic physical balances, larger smoothing of predicted fields and physically inconsistent energy spectra [Bonavita, 2024]. In contrast to physics-based models, where underlying physical laws and numerical discretisation schemes offer interpretability of the simulated processes and potential sources of errors, data-driven DL models lack explicit mechanisms for explaining their predictions. Therefore, understanding and attributing forecast errors is essential for enhancing the performance of DL-based weather forecasting systems.

Forecast errors can arise from poor initial conditions and grow due to chaotic weather dynamics. Error growth is further accelerated due to model limitations, which expedite the divergence of the actual and forecasted trajectories. In classical models, this includes errors associated with numerical and physical approximations [Bauer et al., 2015], which become most evident in intense cyclogenesis, tropical-to-extratropical cyclone transitions, mesoscale convective systems, processes in the tropics, etc. DL model errors, in contrast, arise due to limitations of the specific model

architecture, loss function and minimisation algorithm (e.g. Subich et al. [2025]), as well as by inheriting training data errors and biases. In physics-based models, error diagnostics can be performed using several methods. Some of the typically used include plotting the forecast error against analysis for different lead times, applying ensemble sensitivity methods (e.g. Torn and Hakim [2008]) or using the relaxation (nudging) technique (e.g. Jung et al. [2014], Magnusson [2017]).

An essential difference between DL and physics-based models is that modern libraries allow DL models to be programmed in an auto-differentiable manner. This means we can calculate the gradient of the model's output with respect to the input fields. Such gradients are, especially in classification tasks, often referred to as saliency maps [Simonyan et al., 2014]. They are an explainable AI tool which can be used to find the region of the input fields to which the error of a chosen set of variables inside the selected output gridpoint domain is most sensitive. This method closely resembles the adjoint sensitivity technique (e.g. Errico [1997]), the difference being that the DL model is fully non-linear. In recent studies, saliency maps have been used to calculate the sensitivity of mid-latitude and equatorial prediction to the input geopotential [Rasp and Thuerey, 2021], the sensitivity of the total precipitation (TP) anomaly to the sea surface temperatures (SST) in Pakistani floods [Chen et al., 2024], saliency analysis of atmospheric rivers [Zhang et al., 2022] or finding the optimal initial conditions to minimise the North American heatwave forecast error [Vonich and Hakim, 2024]. Saliency maps could be a helpful tool for identifying potential problems such as model predictions being influenced by processes which, based on our physical understanding, should not play a role (e.g. overreaching region of influence in 850 hPa temperature prediction [Rasp and Thuerey, 2021]), as well as for potentially finding new physics.

The sources of forecast errors in DL weather prediction models have not yet been thoroughly analysed, and the findings from such research could expedite their development. In this research, we analyse the physical consistency of saliency maps of our convolutional encoder-decoder model, ConvCastNet, and develop the relaxation method, where we regionally nudge the predicted fields towards the actual weather state and identify the influence on subsequent forecasts. We then demonstrate how the relaxation technique inherently relates to the model's sensitivity to input fields. We argue that the combination of the two can be used to further the understanding of the sources of errors in DL weather prediction.

The structure of the paper is as follows. Section 2 describes the ConvCastNet model. In section 3, we provide the saliency map calculation methodology and the relaxation technique's implementation. This is followed by results in section 4 and a discussion in section 5.

2 ConvCastNet

All experiments in this paper are conducted using the convolutional encoder-decoder neural network, ConvCastNet (Figure 1), based on the U-Net architecture [Ronneberger et al., 2015]. It consists of 9 neural network blocks, each containing 4 sub-blocks, where depthwise separable (DS) convolutional layers [Sifre and Mallat, 2014] operate on the spherically padded input fields and are followed by the leaky rectified linear unit (Leaky ReLU) activation function and 2D batch normalisation. Blocks are separated by max pooling and transposed convolution operators, and the output fields are obtained from the 9th block using the 2D pointwise convolution. DS convolutions are used inside the sub-blocks due to their significantly reduced number of trainable parameters, compared to classical convolutional layers, while retaining the ability to learn both spatial and channel-wise connections. This reduces the model's variance and improves its ability to generalise outside of training data. All depthwise convolutions except for the first convolution in the first block use a kernel size of 3×3 . The size of the kernel dictates the size of the region in the input field covered by the convolutional kernel. The first depthwise convolution, operating on the input tensor, uses a kernel size 7×7 which corresponds to a $21^\circ \times 21^\circ$ area in order for each kernel to be able to learn synoptic scale spatial patterns. The Leaky ReLU activation function was selected due to its empirically demonstrated effectiveness in improving model performance across our experimental evaluations. To reduce the problem of vanishing or exploding gradients during backpropagation, ConvCastNet is equipped with an encoder-decoder and shared source skip connections (Figure 1). Input tensors are padded using the so-called *spherical padding* (Figure 2), which is designed to ensure that convolutional kernels cover a compact patch of Earth's surface, even if the kernel is positioned on the spatial boundary of the input tensor. The adverse effects of changes in the input distributions during training, i.e., covariate shift, are mitigated by batch normalisation. Our model has a total of 88,354,364 weights.

We train the model using Adam optimiser [Kingma and Ba, 2017] with batch size 5 and starting learning rate 0.001. In addition, we utilise the ReduceLROnPlateau scheduler to adapt the learning rate during training. Specifically, the learning rate is reduced by a factor of 1/100 following six epochs without observable improvement in the loss function. The loss function is $0.1 \cdot \text{MSE}(y_{0,1,\dots,n}, \hat{y}_{0,1,\dots,n})^{\frac{1}{256}}$, with MSE denoting the mean squared error, $y_{0,1,\dots,n}$ denoting n consecutive target and $\hat{y}_{0,1,\dots,n}$ n consecutive model prediction tensors. We change n from 1 to 4 during training, thus

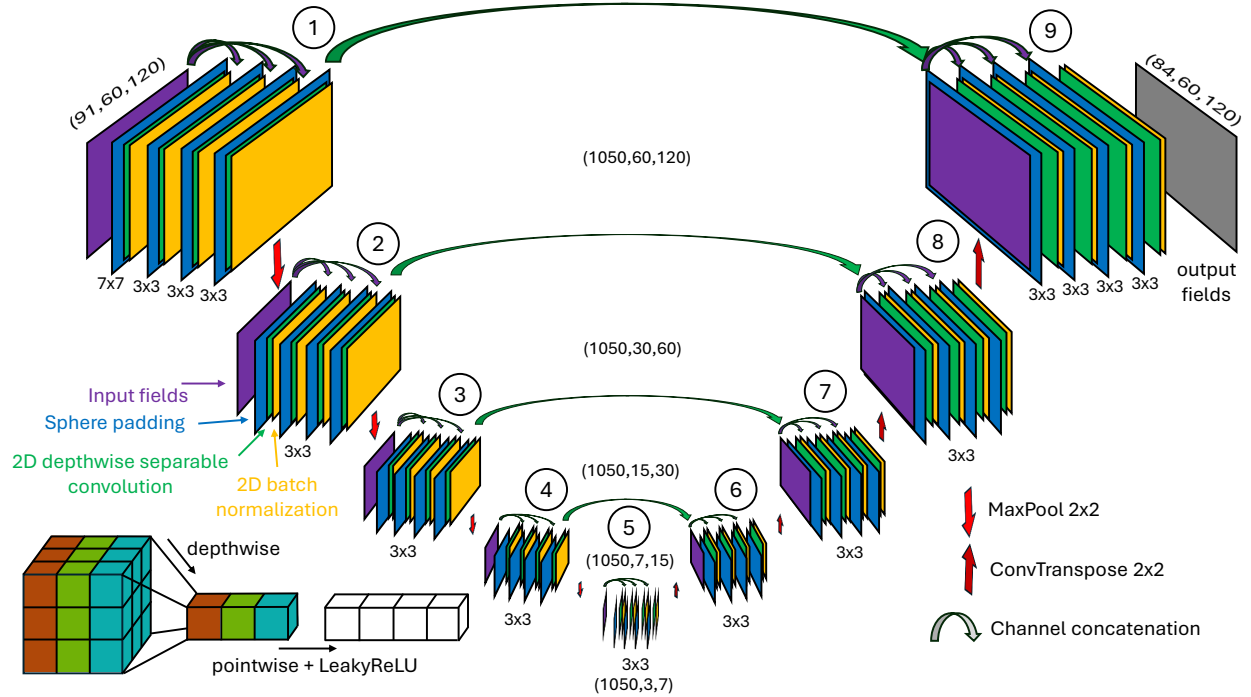


Figure 1: Schematics of ConvCastNet architecture. Coloured layers, positioned in the 9 model blocks, represent input and latent tensors. Specifically, violet colour layers represent input tensors of a given block, dark blue layers show spherically padded tensors, green layers are DS convolutions with Leaky ReLU activation, and orange layers are batch-normalised outputs of green layers. DS convolutions are illustrated in the bottom left corner. The left cube represents a part of the input tensor covered by the DS convolutional kernel of size $(3, 3, 3)$; the middle column shows features after the depthwise convolution, and the right column shows features after the pointwise (1×1) convolution and activation. Max pool and transposed convolution operations are shown using down and up arrows, respectively. Skip connections are plotted as curved arrows and show which tensor is concatenated to which in the channel dimension. Intermediate tensor dimensions are printed above skip connections and below the bottom-most layer. The output fields are plotted in grey.

gradually increasing the number of autoregressive steps used for error minimisation. The MSE exponent was treated as a hyperparameter, and the value $1/256$ was empirically determined to produce the best results on the validation dataset.

Training data is sourced from the ERA5 reanalysis [Hersbach et al., 2020], using the 00 and 12 UTC time instances. It is interpolated to a 3-degree lat-lon grid using a bicubic spline interpolator [Bellman et al., 1973]. Additionally, we exclude the poles from the data due to their redundancy, thus making the grid cover the latitudes between $\varphi = \pm 88.5^\circ$. Data variables and properties are listed in Table 1. The input to the model consists of 15 variables, 8 of which are prognostic. The sea-ice concentration (sic), snow and volumetric soil water (vsm) are persistent throughout the forecast rollout. Their inclusion as static variables likely improves the medium-range weather forecast; however, it makes the model less suitable for long-range forecasting [Cohen et al., 2019]. Latitudes, land-sea mask, and elevation above sea level are also used as static variables, while top-of-atmosphere incident solar radiation (TOASR) changes spatially and temporally, consistent with the date and time of the forecast lead time. The pressure level variables are predicted at 14 pressure levels.

Training data is separated into training, validation and testing subsets, with the latter covering the 2020-2022 time span. The number of autoregressive steps n , the number of epochs and the time interval for training and validation subsets are printed in Table 2. At each stage, we save the model with the highest anomaly correlation coefficient (ACC) on the validation dataset and use it to initialise the weights for the next stage. Data is normalised as

$$\mathcal{S}(X) = \frac{X - \bar{X}}{\text{std}(X) + \varepsilon}, \quad (1)$$

where we denote climatological mean state using \bar{X} , climatological standard deviation using $\text{std}(X)$ and parameter for improved numerical stability $\varepsilon = 10^{-7}$. The time period 1950-2014 is used to evaluate climatological mean and

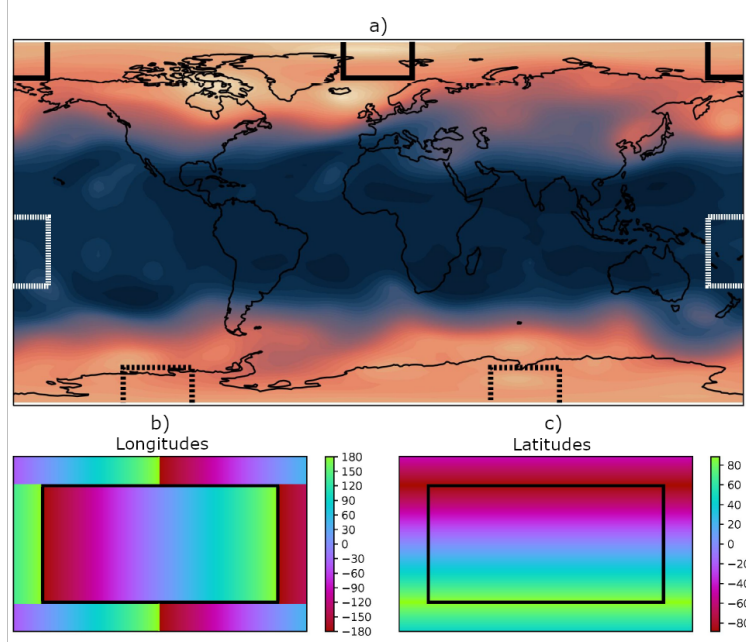


Figure 2: Figure (a) illustrates the spatial regions that convolutional kernels must cover in order to overlap a compact ground patch on the sphere. The white dashed box highlights the coverage near the antimeridian boundary. The black dashed box shows the corresponding region near the south pole, away from the antimeridian, while the solid black box indicates the coverage near the north pole at the antimeridian. Figures (b) and (c) display the longitude and latitude arrangements of the padded tensors designed to meet these coverage requirements.

Table 1: Meteorological data used for ConvCastNet training. Note that 50, 100, ..., 1000 means 13 pressure levels 50, 100, 150, 200, 250, 300, 400, 500, 600, 700, 850, 925, 1000

Variable name	Annotation	Single level	Pressure levels	Input	Output
geopotential	ϕ		50, 100, ..., 1000	✓	✓
specific humidity	q		50, 100, ..., 1000	✓	✓
temperature	T	surface, 2 m	50, 100, ..., 1000	✓	✓
zonal wind	u	10 m	50, 100, ..., 1000	✓	✓
meridional wind	v	10 m	50, 100, ..., 1000	✓	✓
omega	ω		50, 100, ..., 1000	✓	✓
mean sea level pressure	mslp			✓	✓
total precipitation	prec			✓	✓
sea-ice cover	sic			✓	
snow depth	snow			✓	
volumetric soil water	vsm			✓	
TOA incident solar radiation	toasr			✓	
latitudes	φ			✓	
land sea mask	lsm			✓	
elevation	z			✓	

standard deviation. With the exception of sea-ice concentration, snow and volumetric soil moisture, where the mean and standard deviation are calculated globally, aggregating over the φ and λ , standardisation is calculated separately for each latitude φ , longitude λ and pressure level p . The input tensors to the ConvCastNet have a shape (91,60,120), and the output tensors (84,60,120). The channel dimensions don't match due to additional input fields (see Table 1). Prediction rollout is calculated autoregressively as $\hat{y}_{t+1} = \mathcal{M}(\hat{y}_t)$, where \hat{y}_t is standardized prediction at time t and $\hat{y}_0 = y_0$. The model is trained to predict $\Delta t = 12$ hr time steps.

Table 2: Chronologically listed training parameters showing the number of autoregressive steps used in loss minimisation n , number of epochs and time intervals for training and validation subsets.

n	epochs	training	validation
1	20	1970-1984	2015-2019
1	20	1985-1999	2015-2019
1	20	2000-2014	2015-2019
2	18	1980-1999	2015-2019
2	20	2000-2014	2015-2019
4	18	1985-1999	2015-2019
4	20	2002-2017	2018-2019

2.1 Forecast skill

The forecast skill of the trained model is assessed using the root mean squared error (RMSE) and anomaly correlation coefficient (ACC) at all lead times up to 14 days. The initial conditions for the model forecasts are obtained from the test dataset, selecting every fifth day and alternating between 00 and 12 UTC initialisation times. Figure 3 shows the average ACC for all output variables (Table 1) and average RMSE for geopotential height Z at 500 hPa ($Z500$) and T at 850 hPa ($T850$). We can loosely distinguish ACC skill as larger for Z , T , u , v , and ST and significantly lower for ω and precipitation. The latter are significantly more challenging to predict due to their high spatio-temporal variability, dominance of small-scale spectral components, and the limited effective resolution of the model. One reason forecasts of Z , T , $T2m$, $mslp$, and ST tend to be more skilful than others lies in their power spectra. These variables generally exhibit less power at shorter wavelengths, which makes them more amenable to accurate prediction by ConvCastNet, given its relatively coarse effective resolution.

All atmospheric variables except ω show longer decorrelation time scales in the stratosphere compared to the troposphere, consistent with the findings of [Domeisen et al., 2020a]. There, the flow is nearly geostrophic and slowly evolving, making the weather patterns more persistent than in the troposphere. This makes it easier for the model to learn the dynamics, making it more skilful.

The pressure level variables, with the exception of T , show a discontinuity in anomaly correlation at the 850 hPa pressure level. This could be the result of the changes in the dynamics in the boundary layer, as well as ConvcastNet learning extrapolation of the weather state below the ground in the ERA5 reanalysis dataset. ACC is greater than 0.6 for lead times up to 8.5 days for $Z500$ and 7.5 days for $T850$ (Figure 3 g2, h2). RMSE also shows ConvCastNet beating the persistence, where predicted weather states are the same as the initial condition, for all lead times, and beating the 1950-2014 climatology for 10 days in $Z500$ and 9 days in $T850$.

2.2 Spatial error distribution

We also assess forecast skill in individual model gridpoints by averaging the errors over the test dataset for the same set of forecast initialisation instances as in Section 2.1. We compute both absolute errors, defined as the absolute difference between the prediction and the target (ERA5 reanalysis), and normalised errors, which are obtained by dividing the absolute errors by the local natural variability. The latter is defined as the standard deviation of the ERA5 reanalysis at the corresponding date and time, calculated over a ± 6 -day window across the years 1950 to 2014. The 6-day window includes only the samples at the specified time of the day. The normalised error informs us of the magnitude of the error compared to the typical weather variability at a given location and time of the year.

The largest absolute errors for geopotential height Z are in mid-to-high latitudes with a peak in the polar stratosphere above approximately 150 hPa (Figure 4a,b). Both u and v show the most significant error around the tropopause (e.g. Dameris [2015]) and also in the lower part of the mid-latitude troposphere, approximately in the regions of a strong subtropical and mid-latitude westerly jets. In the temperature field, we see an enlarged error at low-level mid-latitudes and in the polar areas, as well as above the tropopause level. The errors in specific humidity (q) are largest in the tropical and subtropical atmosphere in the regions with high moisture content, particularly over the oceans. While the moisture content decreases exponentially with height, the errors in humidity reach a maximum at approximately 850 hPa and decrease rapidly with increasing elevation. The temperature shows large errors in the lower mid-latitude and polar troposphere. This is likely related to baroclinic instability. A local temperature error hotspot is observed in the lee of the Rocky Mountains, possibly indicating inaccuracies in warm and cold advection and front evolution in the wake of lee cyclogenesis. The errors in ω peak in the regions of intense cyclogenesis (e.g. in the Northern Atlantic and

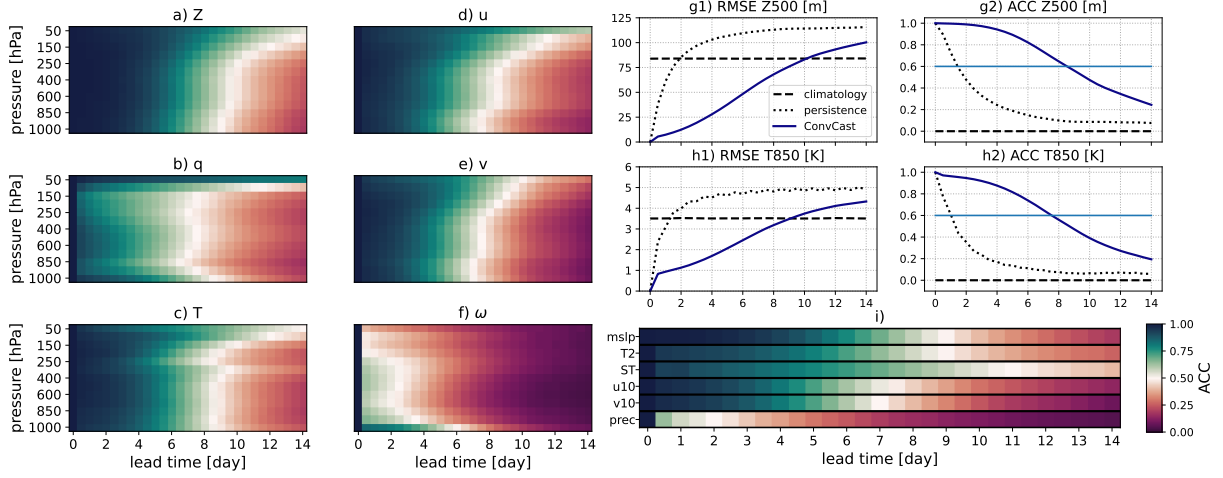


Figure 3: ACC at different lead times and pressure levels for a) Z , b) q , c) T , d) u , e) v , f) ω . ACC for different lead times for i) mean sea level pressure (mslp), 2 m temperature (T2), surface temperature (ST), 10 m zonal wind (u10), 10 m meridional wind (v10) and precipitation (prec), and g1) globally averaged RMSE for 500 hPa geopotential (Z500), g2) ACC for Z500, h1) RMSE for 850 hPa temperature (T850) and h2) ACC for T850. The colour bar for anomaly correlation coefficient is shown at the bottom right. In figures g1, g2, h1, and h2, we plot the forecast skill of ConvCastNet prediction with solid, persistence with dotted, and climatology with a dashed line.

Northern Pacific), the inter-tropical convergence zone (ITCZ) and broadly above continents. Across all variables, we observe that regions with greater natural variability tend to exhibit larger absolute errors (not shown).

Errors (Figure 4c,d), normalised by the natural variability show different spatiotemporal distributions. On lead day 2 (shown), we mainly observe an increased error in the tropical regions and the stratosphere. As only the lower part of the stratosphere is represented in our model, and the 50 hPa level essentially represents the model top, fast error growth might be expected. Furthermore, ML models often struggle more with the representation of the stratosphere than the physics-based models [Lam et al., 2023]. On the other hand, the fast error growth in the tropics is fully aligned with that in physical models. Nevertheless, we speculate that the skill could be improved by usage of date and time-specific gridpoint standardization, where minor perturbations would result in a more significant residual on the loss function. Figure 4 is qualitatively representative for approximately the first 7 days. After that, the tropical tropospheric normalised error saturates near 1 while normalized stratospheric errors near the poles grow to approximately 1.5 for Z , q , T , u , and 1.2 for v and ω (see the distribution of normalized errors after 10 days depicted Figure 13). After 14 days, the most significant normalised errors are in the equatorial stratosphere for Z , q , and u and in the polar stratosphere for T . Interestingly, v and ω show a more homogeneous distribution.

3 Methodology

This study aims to implement the gridpoint relaxation method for DL model error diagnostics and analyse its impact on model predictions, as well as to study the sensitivity of model prediction errors to the initial conditions using the saliency maps [Simonyan et al., 2014].

3.1 Gridpoint relaxation technique

Relaxation or nudging technique in traditional physics-based models involves adding a term $-(1/\tau)(X - X_{\text{ref}})$ to model tendency equations to force the state X towards a reference value X_{ref} , with parameter τ controlling the strength of the nudging. Different forms of nudging, e.g. the spectral nudging, have also been applied recently in hybrid physics-ML models [Husain et al., 2024]. Instead of adding an extra term to the model tendency equation, we implement DL relaxation by directly forcing the model fields. Specifically, we introduce a relaxation weight, Λ , and compute the new time step as a weighted linear combination of the value predicted by the model and the ground truth

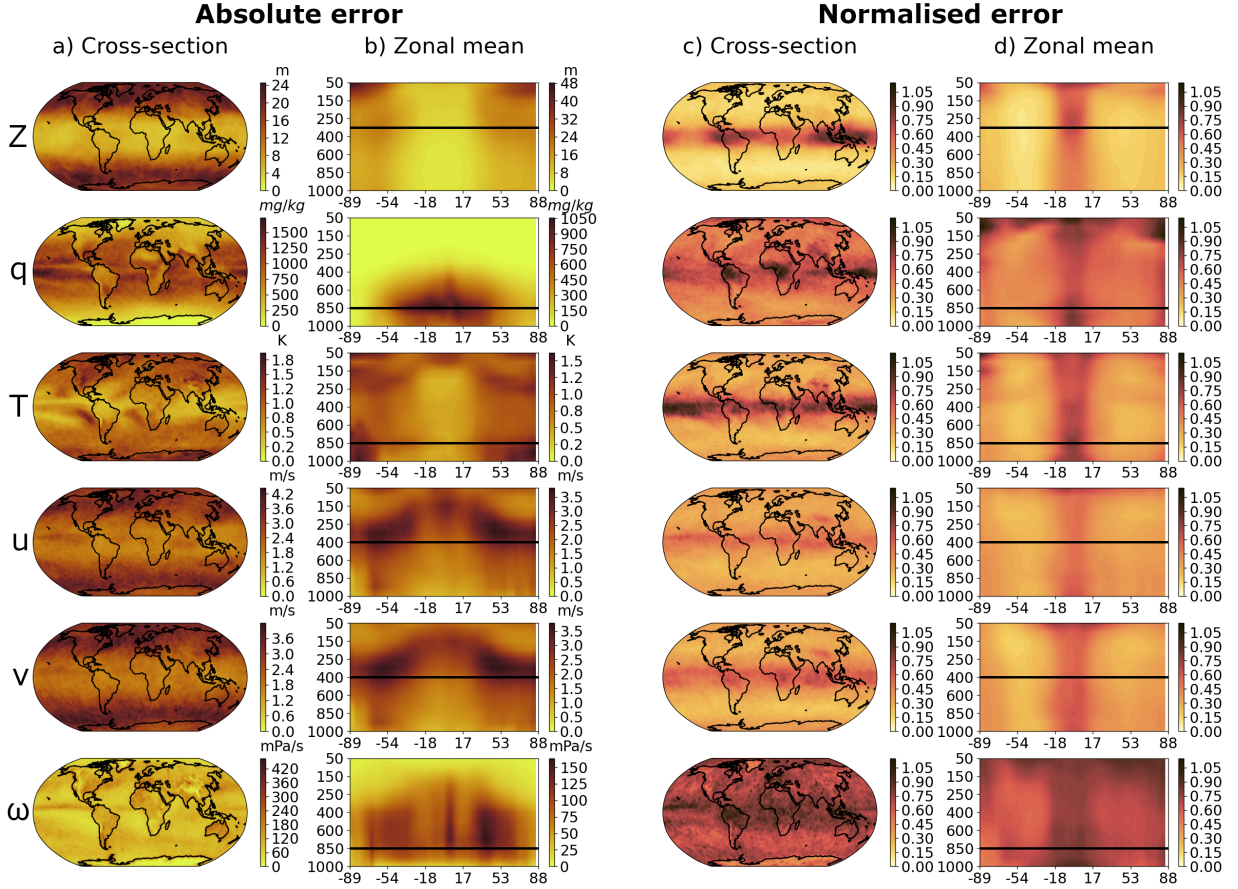


Figure 4: Average absolute (columns a and b) and normalised (columns c and d) errors for predictions at lead day 2. Different rows show errors for Z (row 1), q (row 2), T (row 3), u (row 4), v (row 5) and ω (row 6). Each figure is accompanied by its colour bar. A vertical cross-section of the error's zonal average is plotted in columns b and d. Columns a and c show a horizontal cross-section at the pressure level denoted by a corresponding black bar in the vertical cross-section.

value based on ERA5 reanalysis:

$$X(\lambda, \varphi, p, t + \Delta t) = \Lambda(\lambda, \varphi, p) \cdot X^f(\lambda, \varphi, p, t + \Delta t) \quad (2)$$

$$+ (1 - \Lambda(\lambda, \varphi, p)) \cdot X^t(\lambda, \varphi, p, t + \Delta t). \quad (3)$$

Here, X denotes a prognostic variable, X^t the ERA5 ground truth, $X^f(t + \Delta t) = \mathcal{S}^{-1}[\mathcal{M}_{t \rightarrow t + \Delta t}(\mathcal{S}[X(t)])]$ the forecast, \mathcal{S} denotes standardisation following Equation (1) and \mathcal{S}^{-1} the destandardisation, i.e. the inverse of the standardisation. If $\Lambda = 1$, prediction only consists of the model's output. Inversely, if $\Lambda = 0$, the prediction is replaced by ERA5 reanalysis, consistent with the lead time. Therefore, this definition of relaxation is convenient for a range of values $\Lambda \in [0, 1]$, and the choice of $\Lambda(\lambda, \varphi, p)$ determines the domain where relaxation is applied. We define the relaxation weight as a function of pressure level and latitude as

$$\Lambda(p) = \pm \frac{1}{2} \tanh \frac{p - p_0}{\Delta p} + \frac{1}{2}, \quad (4)$$

and

$$\Lambda(\varphi) = \frac{1}{2} \tanh \frac{\varphi - \varphi_{\max}}{\Delta \varphi} - \frac{1}{2} \tanh \frac{\varphi - \varphi_{\min}}{\Delta \varphi} + 1. \quad (5)$$

The tangens hyperbolicus functions are applied to provide a smooth transition from the relaxation zone to the freely evolving region with Δp and $\Delta \varphi$ determining the width of the transition area in vertical and meridional directions, and p_0 , φ_{\min} and φ_{\max} are the locations of transition, where $\Lambda = 0.5$.

In this study, we investigate the effect of applying relaxation to three regions exhibiting rapid error growth and evaluate how such corrections influence the predictability of midlatitude weather in the medium range. (1) The equatorial region ($\varphi_{\min} = 19.5^\circ\text{S}$, $\varphi_{\max} = 19.5^\circ\text{N}$, $\Delta\varphi = 4.5^\circ$) was selected based on the results of previous studies showing the error growth originating from the small subsynoptic scales in the Tropics [Žagar et al., 2017] and spreading to midlatitude synoptic scales [Žagar, 2017]. Here we relax all prognostic variables, including mslp and precipitation. (2) We test the impact of the surface and boundary layer on forecast skill in the upper troposphere and stratosphere. Here, the relaxation was performed below the boundary pressure level using $p_0 = 850 \text{ hPa}$ and $\Delta p = 100 \text{ hPa}$ and a negative sign in Eq. (4), which was determined based on the aforementioned observed discontinuity in forecast skill (see figure 3). Here, we also apply relaxation in the fields of mslp, surface and 2 m T, and 10 m u and v. Precipitation is not relaxed, as it is influenced by the broader state of the troposphere. (3) The impact of correct stratosphere representation on the tropospheric forecast skill has been the subject of a number of studies (e.g. Domeisen et al. [2020a,b], Kautz et al. [2020]). We test it in the DL weather model by performing relaxation only above the dynamically determined thermal tropopause level, using $\Delta p = 100 \text{ hPa}$ and a positive sign in Eq. (4) as the transition zone. The dynamical thermal tropopause was identified by first interpolating the temperature profile above each grid point to pressure levels using a cubic spline interpolator. The derivative of the interpolated temperature was then computed to locate extrema. Roots of this derivative were identified, and the level corresponding approximately to the expected tropopause altitude based on all of the local maxima, minima and the derivative at 50 hPa was selected. Finally, a Gaussian filter with a standard deviation of 2 was applied in the horizontal spatial dimensions to smooth the tropopause pressure level field and mitigate outlier effects.

We analysed the differences between freely evolving model predictions and the predictions following relaxation for statistically significant changes in absolute errors (Eq. (7)) using the Mann-Whitney U test [Mann and Whitney, 1947]. A 95 % confidence level was used to determine the change as statistically significant. The tests were conducted separately for the vertically and zonally averaged absolute errors of the standardised fields, using forecasts from the test dataset initialised every five days, alternating between the 00 and 12 UTC initial conditions.

Additionally, we calculate the relative error change, defined as

$$\text{relative error change} = \frac{\text{error with relaxation}}{\text{error without relaxation}} - 1, \quad (6)$$

where "error with relaxation" and "error without relaxation" refer to the vertically or zonally averaged absolute errors of the prediction at a given lead time, with and without relaxation, respectively.

3.2 Error sensitivity

We analyse the sensitivity of the model's prediction errors to the initial conditions by computing the error gradient, i.e. the saliency map. We define the error E as a sum of absolute differences between standardised reanalyses and model prediction over a set \mathcal{V} of atmospheric variables in a specified domain \mathcal{D} :

$$E = \sum_{v \in \mathcal{V}} \sum_{(\lambda, \varphi, p) \in \mathcal{D}} |S_v^t(\lambda, \varphi, p, t) - S_v^f(\lambda, \varphi, p, t)| \quad (7)$$

$$= \sum_{v \in \mathcal{V}} \sum_{(\lambda, \varphi, p) \in \mathcal{D}} |S_v^t(\lambda, \varphi, p, t) - [\mathbf{M}_{0 \rightarrow t}(\mathbf{S}(t=0))]_v(\lambda, \varphi, p)|, \quad (8)$$

where \mathcal{D} represents a closed volume of atmosphere for which the sensitivity is calculated, $\mathcal{V} = \{\phi, q, T, u, v, \omega\}$ is the set of atmospheric variables, included in the error calculation, $S^t = \mathcal{S}(\bar{X}^t)$ is the standardised ERA5 ground truth and $S^f = \mathcal{S}(X^f)$ is the standardised predicted tensor. We use bold letter \mathbf{S} to represent a standardised tensor with all variables and spatial dimensions. Using the DL model's auto-differentiability, we can then compute the error gradient with respect to the initial condition as

$$\frac{\partial E}{\partial \mathbf{S}(0)} = - \sum_{v \in \mathcal{V}} \sum_{(\lambda, \varphi, p) \in \mathcal{D}} \text{sgn}(S_v^t(\lambda, \varphi, p, t) - [\mathbf{M}_{0 \rightarrow t}(\mathbf{S}(0))]_v(\lambda, \varphi, p)) [\nabla_{\mathbf{S}(0)} \mathbf{M}_{0 \rightarrow t}(\mathbf{S}(0))]_v(\lambda, \varphi, p), \quad (9)$$

where the term $\nabla_{\mathbf{S}(0)} \mathbf{M}_{0 \rightarrow t}(\mathbf{S}(0)) = \partial \mathbf{M}_{0 \rightarrow t}(\mathbf{S}(0)) / \partial (\mathbf{S}(0))$ represents the sensitivity of the model output at time t to changes in the initial condition $\mathbf{S}(0)$ and is computed using backpropagation. The sign function is defined as

$$\text{sgn}(x) = \begin{cases} 1, & \text{if } x \geq 0 \\ -1, & \text{if } x < 0 \end{cases} \quad (10)$$

to denote the sign function. Except for the sign, the resulting gradient is the same as the gradient of the model's prediction.

We calculate the absolute error sensitivity (AES) for two case studies. First, we calculate Hurricane Ian's tropical-to-extratropical transition AES to initial conditions at lead times 6, 8, 10 and 12 days and qualitatively analyse its physical consistency. The domain \mathcal{D} is chosen to include the cyclone and the surrounding region of the most significant prediction error. The forecast is initiated on September, 23rd, 2022 at 00 UTC.

Second, we calculate the AES in the testing dataset for the absolute error sum in three domains;

1. $\mathcal{D}_A = \{(\varphi, \lambda, p); \varphi \in [-4.5, 4.5]^\circ\},$
2. $\mathcal{D}_B = \{(\varphi, \lambda, p); \varphi \in [28.5, 34.5]^\circ\},$
3. $\mathcal{D}_C = \{(\varphi, \lambda, p); \varphi \in [40.5, 49.5]^\circ\},$

in each case using $\lambda \in [0, 360]^\circ$ and pressure levels $p \in \{1000, 925, 850, 700, 600\}$ hPa. In the error calculation, we also include precipitation, mslp, surface (T_s) and 2 m (T_2) temperature, and 10 m zonal (u_{10}) and meridional (v_{10}) wind.

4 Results

4.1 Gridpoint relaxation

First, we look at the relative error change in the temperature predictions for all three cases (fig. 5). In the first case, i.e. the tropics, statistically significant relative error reduction is mainly observed in immediate proximity to the tropical relaxation domain, slowly spreading in a meridional direction. After 8 days, the relaxation influence reaches approximately $10 - 15^\circ$ North and South from the $\Lambda = 0.5$ relaxation domain boundary. In the vertical profile of the zonally averaged error change (5) b), we see the relaxation influence spreads towards the poles unevenly, with greater reach roughly between 100 and 500 hPa. Tropical relaxation doesn't seem to reach mid-latitudes and polar regions, where we, on average, don't observe any improvement or, regionally, up to approximately 5 % better forecast with no statistically significant trend.

In the second case, i.e. the boundary layer, we observe the influence spreading in the bottom-up direction, mainly being channelled towards the mid-latitude jet stream and later enveloping the tropical atmosphere. The influence of relaxation is more prominent above the oceans in the regions with high baroclinic activity. While we observe statistically significant changes in the lower troposphere in ITCZ, we see an inhibited spread to the tropical mid-troposphere. The most prominent influence is observed in the Southern Hemisphere.

In the third case, i.e. the stratosphere, the influence of relaxation is most extensive. Significant improvement is observed globally at lead day 2, becoming even more prominent with increasing lead time, with the largest vertically averaged error improvement reaching 75 %. The influence is most significant near the mid-latitude stratosphere and slowly decreases towards the ground and the equator. In all cases, the region of influence doesn't spread much further, even at lead day 14 (not shown).

Second, we compare the relative error change for different variables. In figure 7, we plot relative error change for Z , q and ω at lead day 4 for the second case, i.e. the boundary layer. In all cases, including the temperature T , u and v (not shown), we see the relaxation exerting the most considerable impact on the mid-latitude troposphere in a bottom-up direction. The magnitude of the effect is different, with a larger influence on Z and T and a lesser one for q and ω . All fields also show a more significant error improvement above mid-latitude oceans, specifically in the highly baroclinic regions of the North Atlantic, North Pacific and the Southern Ocean. Additionally, we see an improved q and ω prediction in the ITCZ, extending to the u and v as well (not shown).

The distinctions primarily arise in the tropical atmosphere. In the T field (figure 5 2 c,d) we mainly observe statistically significant improvement in the lower troposphere and the stratosphere and almost no change in the mid-troposphere. In the field of q and ω , we observe to some extent the opposite effect, where the mid-troposphere improves the most, with a lesser impact on the surrounding regions. The relative error change in Z significantly improves near the boundary layer but retrogrades in and above the mid-troposphere.

4.2 Error sensitivity

First, we look at a case study of the AES for Hurricane Ian's predicted tropical-to-extratropical cyclone transition (figure 9). On the morning of September 23, approximately at the time of the forecast initialisation, the later Hurricane Ian formed as a tropical depression in the central Caribbean [National Weather Service, 2022]. The absolute errors associated with Hurricane Ian tightly enveloped the hurricane for the first eight days (figure 9 a)). After this time, the predicted path loses connection to the observed track, where the westerly jet redirects the cyclone's path to the

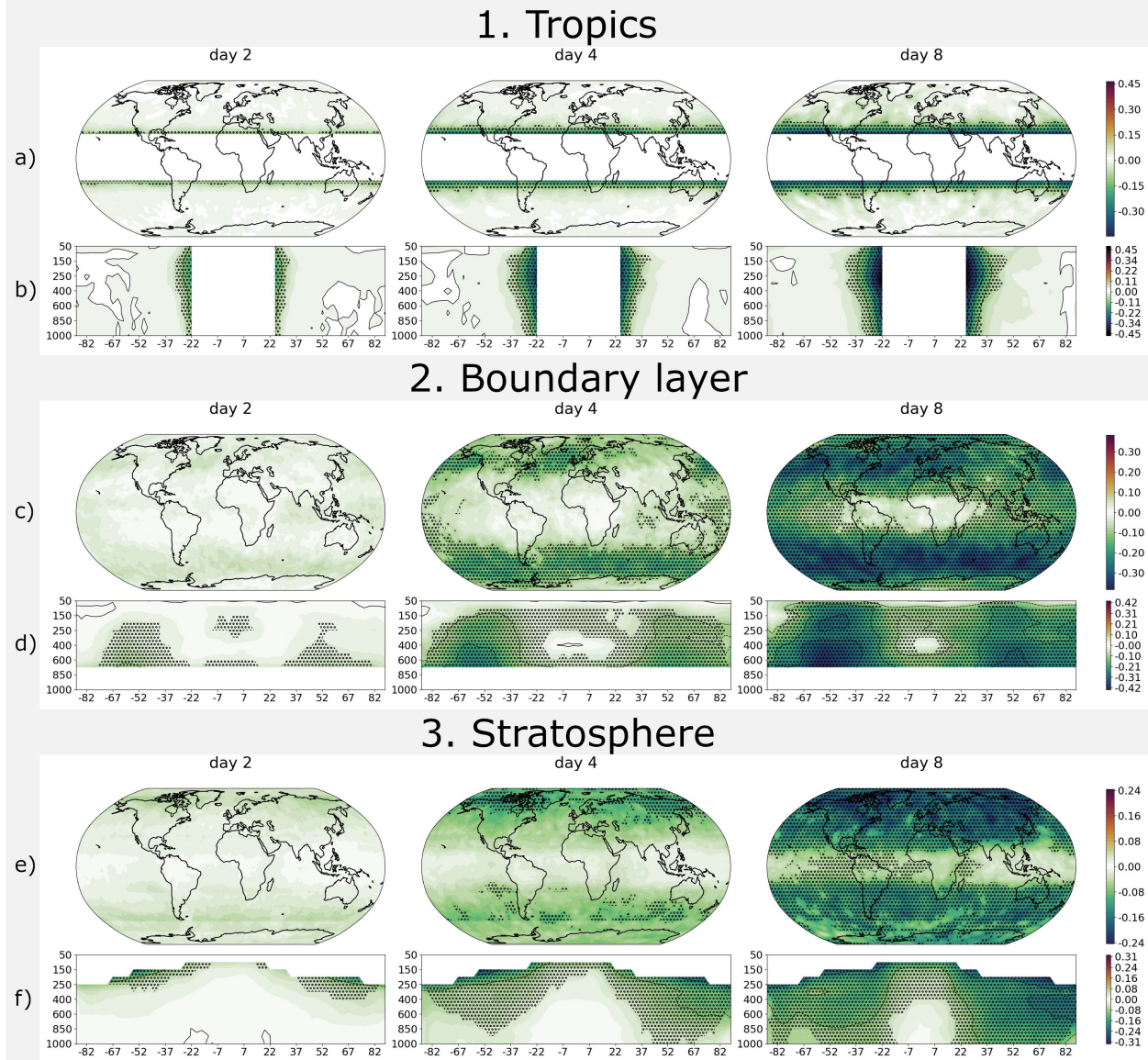


Figure 5: First panel shows the relative temperature error change for the relaxation in the tropics (case 1), panel 2 depicts it for the boundary layer relaxation (case 2) and panel 3 showcases it for the stratosphere relaxation (case 3). Plots (a, c, e) show vertically-averaged change in temperature relative error and panels (b, d, f) show the pressure-latitudinal cross-section of relative error change. Negative values indicate reduction in relative error. The contour spacing in (b,d,f) is 0.1. Statistically significant changes are hatched with black circles. Relaxation zones are masked white and indicate areas with relaxation parameter $\Lambda > 0.5$.

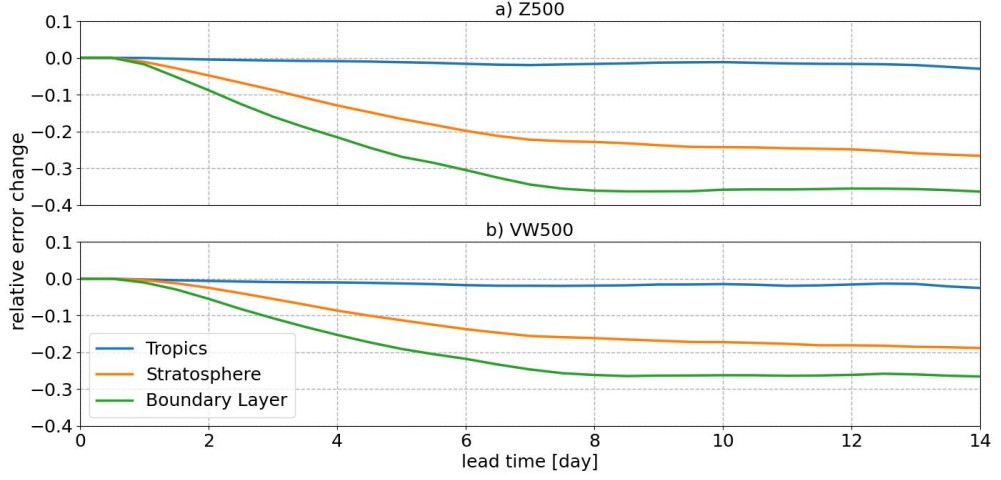


Figure 6: Relative error change (equation (6)) for Z500 (a) and 500 hPa vector wind VW500 (b). The error is defined as RMSE, where squared errors are averaged over all of the forecasts and spatial dimensions.

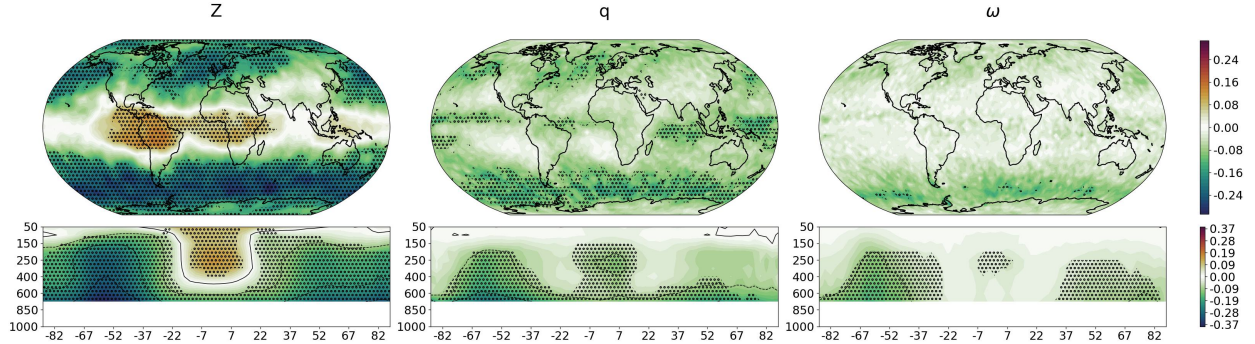


Figure 7: Same as figure 5 for lead time of 4 days, but for boundary layer relaxation relative error change in the fields of geopotential height Z , specific humidity q and omega ω .

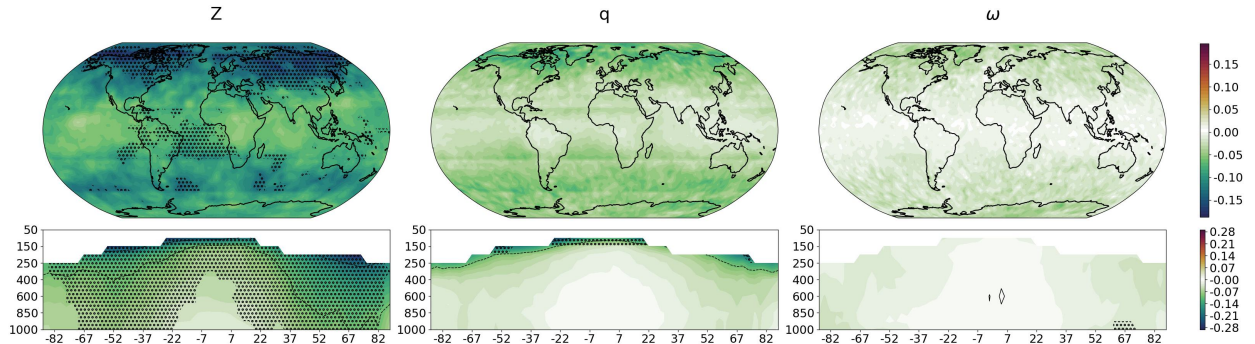


Figure 8: Same as figure 7 but for stratosphere relaxation.

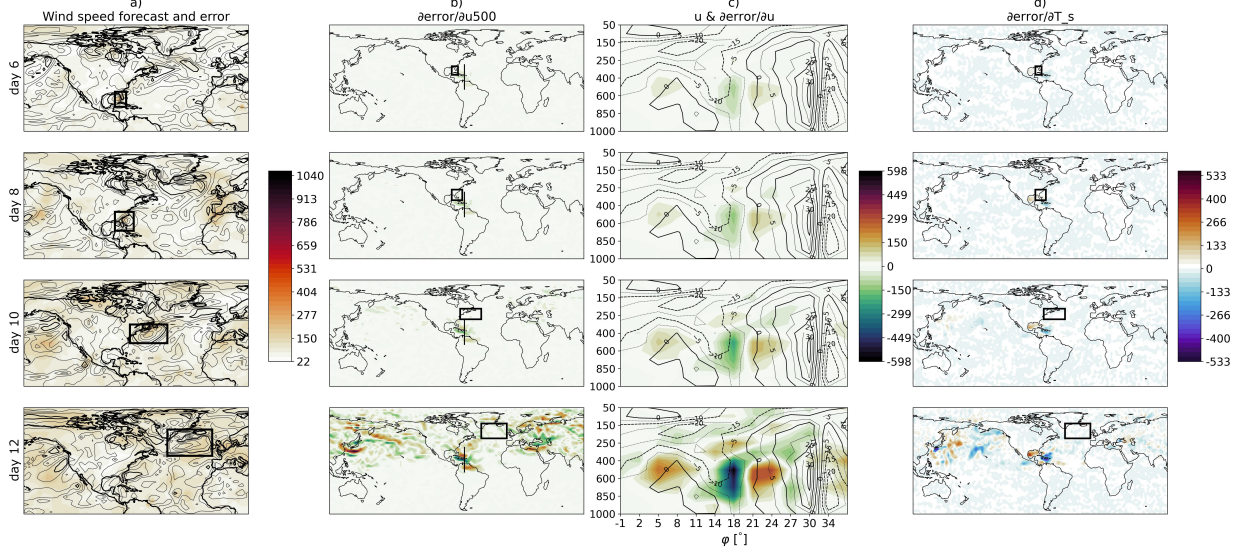


Figure 9: In column a), we show the 10 m horizontal wind magnitude $\sqrt{u_{10}^2 + v_{10}^2}$ prediction (contours) and absolute error sum over all variables and pressure levels (colours) $\forall \varphi, \lambda$. In b), we show the error sensitivity to the 500 hPa u . In c), we plot the vertical cross-section of u (contours) and error sensitivity to u (colours) at $\lambda = -69^\circ$ and $\varphi \in [-1.5^\circ, 40.5^\circ]$ (the black line in b)), and in d) we plot absolute error sensitivity to T_s . Row 1 shows 6th, row 2 8th, row 3 10th and row 4 12th day AES to initial conditions. Black boxes show the error calculation domain \mathcal{D} (see eq. 7). Colorbar for b) and c) is next to c), and contours in a) are $\Delta u = 2.5$ m/s apart with bold contours at 10, 20, and 30 m/s.

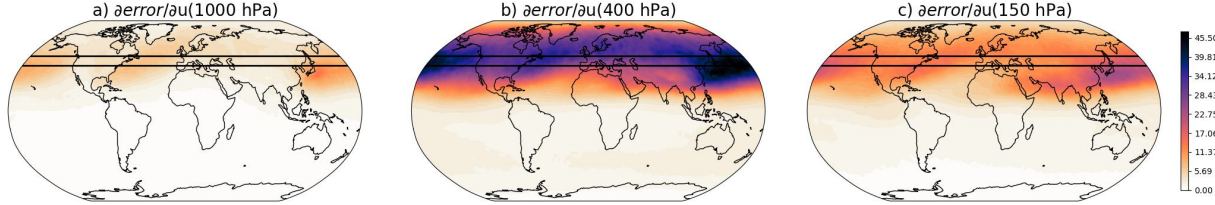


Figure 10: The 2020-2022 average AES in domain \mathcal{D}_C (volume between the black lines) to zonal wind u for lead day 8 and three different pressure levels. In Figure a), we show the AES at 1000, b) 400 and c) 150 hPa.

Northern Atlantic. For the first 8 days, figure 9 b) and c) shows the AES to the zonal wind being mostly confined to the Caribbean's mid-troposphere. After 10 and 12 days, AES spreads upstream to the Northern and Western Pacific, Asia and Europe. The AES diminishes towards the equator and the pole and, for the most part, doesn't reach over the equator to the Southern Hemisphere. In the vertical cross-section, we observe an amplification of the sensitivity to the initial mid-tropospheric zonal wind and it's spreading to the stratosphere. The error exerts only a limited sensitivity to Hurricane Fiona, which at the initial conditions time was located downstream of Hurricane Ian, at $\varphi = 30^\circ$ (see 9 c)). The error sensitivity to surface temperature shows a similar pattern, with the short-term influence localised in the Caribbean and the Bay of Mexico and the long-term influence spreading upstream to the Northern and Western Pacific and, to some extent, the Mediterranean and Black Sea. The model is sensitive primarily to the sea T_s and much less the land and ice surface temperature.

Second, we look at the 2020-2022 average error sensitivity for different pressure levels (fig. 10). We see both the difference in magnitude and the distribution of error sensitivity. Mostly, the AES sensitivity is confined to the Northern Hemisphere. Two regions of local maximum sensitivity are located at Asia and North America's highly baroclinic eastern flanks. The sensitivity diminishes towards the West coasts of North America and Europe and is more minor over the continents.

In figure 11, we examine the changes in sensitivity for the T_s at two different forecast times. The model is mostly sensitive to the T_s over the seas, i.e. the sea surface temperature (SST), and exerts only limited sensitivity over the land and ice T_s . In the shorter forecast, we see a more confined region of sensitivity, mostly to the areas underneath and slightly to the south of the \mathcal{D}_C domain. The southernmost AES regions at 4-day predictions reach down to the Bay

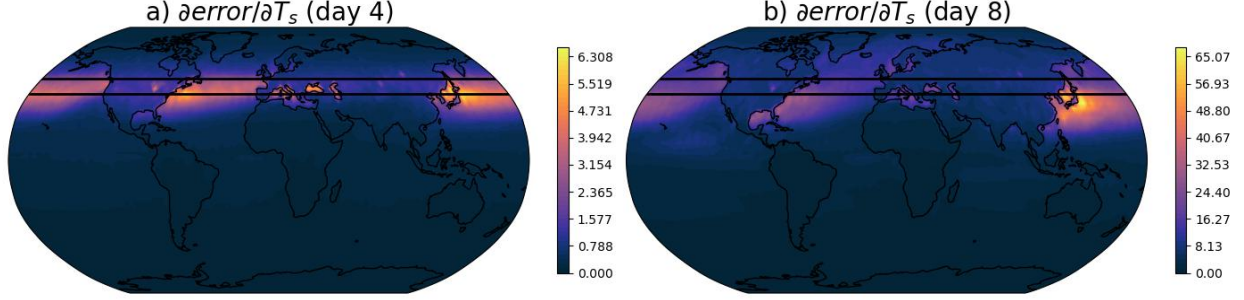


Figure 11: Same as figure 10 but for T_s with a) 4 and b) 8-day predictions.

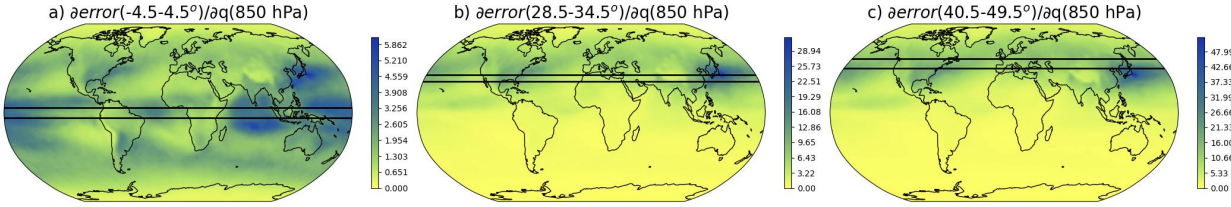


Figure 12: Same as figure 10 but for 850 hPa q with domains a) \mathcal{D}_A , b) \mathcal{D}_B and c) \mathcal{D}_C .

of Mexico and the East Chinese Sea. The AES of the 8-day prediction increases in magnitude and spreads further to the North and South. We see an increased sensitivity to the Arctic seas and an increase in the sensitivity to the Bay of Mexico, the Eastern Pacific and the South Chinese Sea.

In figure 12, we compare the error sensitivity to the 850 hPa q for different error domains. The domains are not the same volume; therefore, a direct quantitative comparison is not possible. Figures b) and c) show considerable sensitivity to the Eastern flanks of the continents, the Central and Eastern North America area, the Ganges and Brahmaputra basins and other regions, including the Pacific ITCZ. When comparing domains \mathcal{D}_B (figure b)) with \mathcal{D}_C (figure c)), only a tiny meridional shift is observed. In Figure a), we see the errors in domain \mathcal{D}_A being sensitive to the tropical area and Northern and Southern Hemispheric mid-latitudes. The largest sensitivity is to the Indian Ocean region, West Pacific and the synoptic mountain leesides.

5 Discussion and Conclusions

In our research, we implement the gridpoint relaxation technique to our optimised convolution encoder-decoder, ConvCastNet. We provide three cases where we nudge the predicted fields in the tropics, boundary layer and stratosphere. We don't see any significant improvement in the mid-to-high latitudes with the relaxation in the tropics. The boundary layer relaxation influences the troposphere and stratosphere in a bottom-up manner, with contradicting effects in the tropical mid-troposphere, where improved q and ω are accompanied by a neutral T and negative Z change. Relaxation in the stratosphere proves to be beneficial for medium-range weather predictions with up to 25 % vertically averaged error improvement at lead day 8.

We also show our model's absolute error sensitivity (AES) to initial conditions, which produces plausible results. The sensitivity patterns align with established physics-based expectations. Specifically, the model's predictions exhibit sensitivity to upstream Rossby wave activity, with longer-range teleconnections emerging at larger forecast lead times. Additionally, the model demonstrates greater sensitivity to variations in sea surface temperature (SST) compared to land or ice surface temperature.

Financial Disclosure

This research was also supported by the University of Ljubljana Grant SN-ZRD/22-27/0510.

References

- M. Andrychowicz, L. Espeholt, D. Li, S. Merchant, A. Merose, F. Zyda, S. Agrawal, and N. Kalchbrenner. Deep learning for day forecasts from sparse observations, 2023. URL <https://arxiv.org/abs/2306.06079>.
- P. Bauer, A. Thorpe, and G. Brunet. The quiet revolution of numerical weather prediction. *Nature*, 525(7567):47–55, Sep 2015. ISSN 1476-4687. doi: 10.1038/nature14956. URL <https://doi.org/10.1038/nature14956>.
- R. Bellman, B. Kashef, and R. Vasudevan. Dynamic programming and bicubic spline interpolation. *Journal of Mathematical Analysis and Applications*, 44(1):160–174, 1973. ISSN 0022-247X. doi: [https://doi.org/10.1016/0022-247X\(73\)90033-4](https://doi.org/10.1016/0022-247X(73)90033-4). URL <https://www.sciencedirect.com/science/article/pii/0022247X73900334>.
- K. Bi, L. Xie, H. Zhang, X. Chen, X. Gu, and Q. Tian. Accurate medium-range global weather forecasting with 3d neural networks. *Nature*, 619(7970):533–538, Jul 2023. ISSN 1476-4687. doi: 10.1038/s41586-023-06185-3. URL <https://doi.org/10.1038/s41586-023-06185-3>.
- C. Bodnar, W. Bruinsma, A. Lucic, M. Stanley, J. Brandstetter, P. Garvan, M. Riechert, J. Weyn, H. Dong, A. Vaughan, J. Gupta, K. Thambiratnam, A. Archibald, E. Heider, M. Welling, R. Turner, and P. Perdikaris. Aurora: A foundation model of the atmosphere. Technical Report MSR-TR-2024-16, Microsoft Research AI for Science, May 2024. URL <https://www.microsoft.com/en-us/research/publication/aurora-a-foundation-model-of-the-atmosphere/>.
- M. Bonavita. On some limitations of current machine learning weather prediction models. *Geophysical Research Letters*, 51(12):e2023GL107377, 2024. doi: <https://doi.org/10.1029/2023GL107377>. URL <https://agupubs.onlinelibrary.wiley.com/doi/abs/10.1029/2023GL107377> e2023GL107377 2023GL107377.
- B. Bonev, T. Kurth, C. Hundt, J. Pathak, M. Baust, K. Kashinath, and A. Anandkumar. Spherical fourier neural operators: Learning stable dynamics on the sphere, 2023. URL <https://arxiv.org/abs/2306.03838>.
- L. Chen, X. Zhong, F. Zhang, Y. Cheng, Y. Xu, Y. Qi, and H. Li. Fuxi: a cascade machine learning forecasting system for 15-day global weather forecast. *npj Climate and Atmospheric Science*, 6(1):190, Nov 2023. ISSN 2397-3722. doi: 10.1038/s41612-023-00512-1. URL <https://doi.org/10.1038/s41612-023-00512-1>.
- L. Chen, X. Zhong, H. Li, J. Wu, B. Lu, D. Chen, S.-P. Xie, L. Wu, Q. Chao, C. Lin, Z. Hu, and Y. Qi. A machine learning model that outperforms conventional global subseasonal forecast models. *Nature Communications*, 15(1):6425, Jul 2024. ISSN 2041-1723. doi: 10.1038/s41467-024-50714-1. URL <https://doi.org/10.1038/s41467-024-50714-1>.
- J. Cohen, D. Coumou, J. Hwang, L. Mackey, P. Orenstein, S. Totz, and E. Tziperman. S2s reboot: An argument for greater inclusion of machine learning in subseasonal to seasonal forecasts. *Wiley Interdisciplinary Reviews: Climate Change*, 10:e00567, 3 2019. ISSN 1757-7799. doi: 10.1002/WCC.567. URL <https://onlinelibrary.wiley.com/doi/full/10.1002/wcc.567> <https://onlinelibrary.wiley.com/doi/10.1002/wcc.567>.
- M. Dameris. Stratosphere/troposphere exchange and structure | tropopause. In G. R. North, J. Pyle, and F. Zhang, editors, *Encyclopedia of Atmospheric Sciences (Second Edition)*, pages 269–272. Academic Press, Oxford, second edition edition, 2015. ISBN 978-0-12-382225-3. doi: <https://doi.org/10.1016/B978-0-12-382225-3.00418-7>. URL <https://www.sciencedirect.com/science/article/pii/B9780123822253004187>.
- D. I. Domeisen, A. H. Butler, A. J. Charlton-Perez, B. Ayarzagüena, M. P. Baldwin, E. Dunn-Sigouin, J. C. Furtado, C. I. Garfinkel, P. Hitchcock, A. Y. Karpechko, H. Kim, J. Knight, A. L. Lang, E.-P. Lim, A. Marshall, G. Roff, C. Schwartz, I. R. Simpson, S.-W. Son, and M. Taguchi. The role of the stratosphere in subseasonal to seasonal prediction: 1. predictability of the stratosphere. *Journal of Geophysical Research: Atmospheres*, 125(2):e2019JD030920, 2020a. doi: <https://doi.org/10.1029/2019JD030920>. URL <https://agupubs.onlinelibrary.wiley.com/doi/abs/10.1029/2019JD030920> 10.1029/2019JD030920 e2019JD030920 10.1029/2019JD030920.
- D. I. V. Domeisen, A. H. Butler, A. J. Charlton-Perez, B. Ayarzagüena, M. P. Baldwin, E. Dunn-Sigouin, J. C. Furtado, C. I. Garfinkel, P. Hitchcock, A. Y. Karpechko, H. Kim, J. Knight, A. L. Lang, E.-P. Lim, A. Marshall, G. Roff, C. Schwartz, I. R. Simpson, S.-W. Son, and M. Taguchi. The role of the stratosphere in subseasonal to seasonal prediction: 1. predictability of the stratosphere. *J. Geophys. Res.*, 125(2), Jan. 2020b.
- R. M. Errico. What is an adjoint model? *Bulletin of the American Meteorological Society*, 78(11):2577 – 2592, 1997. doi: 10.1175/1520-0477(1997)078<2577:WIAAM>2.0.CO;2. URL https://journals.ametsoc.org/view/journals/bams/78/11/1520-0477_1997_078_2577_wiaam_2_0_co_2.xml.
- H. Hersbach, B. Bell, P. Berrisford, S. Hirahara, A. Horányi, J. Muñoz-Sabater, J. Nicolas, C. Peubey, R. Radu, D. Schepers, A. Simmons, C. Soci, S. Abdalla, X. Abellan, G. Balsamo, P. Bechtold, G. Biavati, J. Bidlot, M. Bonavita, G. De Chiara, P. Dahlgren, D. Dee, M. Diamantakis, R. Dragani, J. Flemming, R. Forbes, M. Fuentes, A. Geer, L. Haimberger, S. Healy, R. J. Hogan, E. Hölm, M. Janisková, S. Keeley, P. Laloyaux, P. Lopez, C. Lupu, G. Radnoti,

- P. de Rosnay, I. Rozum, F. Vamborg, S. Villaume, and J.-N. Thépaut. The era5 global reanalysis. *Quarterly Journal of the Royal Meteorological Society*, 146(730):1999–2049, 2020. doi: <https://doi.org/10.1002/qj.3803>. URL <https://rmets.onlinelibrary.wiley.com/doi/abs/10.1002/qj.3803>.
- S. Z. Husain, L. Separovic, J.-F. Caron, R. Aider, M. Buehner, S. Chamberland, E. Lapalme, R. McTaggart-Cowan, C. Subich, P. A. Vaillancourt, J. Yang, and A. Zadra. Leveraging data-driven weather models for improving numerical weather prediction skill through large-scale spectral nudging, 2024. URL <https://arxiv.org/abs/2407.06100>.
- T. Jung, M. A. Kasper, T. Semmler, and S. Serrar. Arctic influence on subseasonal midlatitude prediction. *Geophysical Research Letters*, 41(10):3676–3680, 2014. doi: <https://doi.org/10.1002/2014GL059961>. URL <https://agupubs.onlinelibrary.wiley.com/doi/abs/10.1002/2014GL059961>.
- L.-A. Kautz, I. Polichtchouk, T. Birner, H. Garny, and J. G. Pinto. Enhanced extended-range predictability of the 2018 late-winter eurasian cold spell due to the stratosphere. *Q. J. R. Meteorol. Soc.*, 146(727):1040–1055, Jan. 2020.
- R. Keisler. Forecasting global weather with graph neural networks, 2022. URL <https://arxiv.org/abs/2202.07575>.
- D. P. Kingma and J. Ba. Adam: A method for stochastic optimization, 2017. URL <https://arxiv.org/abs/1412.6980>.
- R. Lam, A. Sanchez-Gonzalez, M. Willson, P. Wirnsberger, M. Fortunato, F. Alet, S. Ravuri, T. Ewalds, Z. Eaton-Rosen, W. Hu, A. Merose, S. Hoyer, G. Holland, O. Vinyals, J. Stott, A. Pritzel, S. Mohamed, and P. Battaglia. Learning skillful medium-range global weather forecasting. *Science*, 382(6677):1416–1421, 2023. doi: 10.1126/science.adi2336. URL <https://www.science.org/doi/abs/10.1126/science.adi2336>.
- S. Lang, M. Alexe, M. Chantry, J. Dramsch, F. Pinault, B. Raoult, M. C. A. Clare, C. Lessig, M. Maier-Gerber, L. Magnusson, Z. B. Bouallègue, A. P. Nemesio, P. D. Dueben, A. Brown, F. Pappenberger, and F. Rabier. Aifs – ecmwf’s data-driven forecasting system, 2024. URL <https://arxiv.org/abs/2406.01465>.
- L. Magnusson. Diagnostic methods for understanding the origin of forecast errors. *Quarterly Journal of the Royal Meteorological Society*, 143(706):2129–2142, 2017. doi: <https://doi.org/10.1002/qj.3072>. URL <https://rmets.onlinelibrary.wiley.com/doi/abs/10.1002/qj.3072>.
- H. B. Mann and D. R. Whitney. On a Test of Whether one of Two Random Variables is Stochastically Larger than the Other. *The Annals of Mathematical Statistics*, 18(1):50 – 60, 1947. doi: 10.1214/aoms/1177730491. URL <https://doi.org/10.1214/aoms/1177730491>.
- National Weather Service. Hurricane ian overview, 2022. URL <https://www.weather.gov/mhx/HurricaneIan093022>. Accessed: 2025-02-04.
- T. Nguyen, J. Brandstetter, A. Kapoor, J. K. Gupta, and A. Grover. Climax: A foundation model for weather and climate, 2023. URL <https://arxiv.org/abs/2301.10343>.
- J. Pathak, S. Subramanian, P. Harrington, S. Raja, A. Chattopadhyay, M. Mardani, T. Kurth, D. Hall, Z. Li, K. Azizzadenesheli, P. Hassanzadeh, K. Kashinath, and A. Anandkumar. Fourcastnet: A global data-driven high-resolution weather model using adaptive fourier neural operators, 2022. URL <https://arxiv.org/abs/2202.11214>.
- I. Price, A. Sanchez-Gonzalez, F. Alet, T. R. Andersson, A. El-Kadi, D. Masters, T. Ewalds, J. Stott, S. Mohamed, P. Battaglia, R. Lam, and M. Willson. Probabilistic weather forecasting with machine learning. *Nature*, Dec 2024. ISSN 1476-4687. doi: 10.1038/s41586-024-08252-9. URL <https://doi.org/10.1038/s41586-024-08252-9>.
- S. Rasp and N. Thuerey. Data-driven medium-range weather prediction with a resnet pretrained on climate simulations: A new model for weatherbench. *Journal of Advances in Modeling Earth Systems*, 13(2):e2020MS002405, 2021. doi: <https://doi.org/10.1029/2020MS002405>. URL <https://agupubs.onlinelibrary.wiley.com/doi/abs/10.1029/2020MS002405>. e2020MS002405 2020MS002405.
- O. Ronneberger, P. Fischer, and T. Brox. U-net: Convolutional networks for biomedical image segmentation, 2015. URL <https://arxiv.org/abs/1505.04597>.
- L. Sifre and S. Mallat. Rigid-motion scattering for texture classification. 03 2014.
- K. Simonyan, A. Vedaldi, and A. Zisserman. Deep inside convolutional networks: Visualising image classification models and saliency maps, 2014. URL <https://arxiv.org/abs/1312.6034>.
- C. Subich, S. Z. Husain, L. Separovic, and J. Yang. Fixing the double penalty in data-driven weather forecasting through a modified spherical harmonic loss function, 2025. URL <https://arxiv.org/abs/2501.19374>.
- R. D. Torn and G. J. Hakim. Ensemble-based sensitivity analysis. *Monthly Weather Review*, 136(2):663 – 677, 2008. doi: 10.1175/2007MWR2132.1. URL <https://journals.ametsoc.org/view/journals/mwre/136/2/2007mwr2132.1.xml>.

- P. T. Vonich and G. J. Hakim. Predictability limit of the 2021 pacific northwest heatwave from deep-learning sensitivity analysis. *Geophysical Research Letters*, 51(19):e2024GL110651, 2024. doi: <https://doi.org/10.1029/2024GL110651>. URL <https://agupubs.onlinelibrary.wiley.com/doi/abs/10.1029/2024GL110651>.
- J. A. Weyn, D. R. Durran, and R. Caruana. Can machines learn to predict weather? using deep learning to predict gridded 500-hpa geopotential height from historical weather data. *Journal of Advances in Modeling Earth Systems*, 11(8):2680–2693, 2019. doi: <https://doi.org/10.1029/2019MS001705>. URL <https://agupubs.onlinelibrary.wiley.com/doi/abs/10.1029/2019MS001705>.
- J. A. Weyn, D. R. Durran, and R. Caruana. Improving data-driven global weather prediction using deep convolutional neural networks on a cubed sphere. *Journal of Advances in Modeling Earth Systems*, 12(9):e2020MS002109, 2020. doi: <https://doi.org/10.1029/2020MS002109>. URL <https://agupubs.onlinelibrary.wiley.com/doi/abs/10.1029/2020MS002109>.
- J. A. Weyn, D. R. Durran, R. Caruana, and N. Cresswell-Clay. Sub-seasonal forecasting with a large ensemble of deep-learning weather prediction models. *Journal of Advances in Modeling Earth Systems*, 13(7):e2021MS002502, 2021. doi: <https://doi.org/10.1029/2021MS002502>. URL <https://agupubs.onlinelibrary.wiley.com/doi/abs/10.1029/2021MS002502>.
- C. Zhang, Z. P. Brodeur, S. Steinschneider, and J. D. Herman. Leveraging spatial patterns in precipitation forecasts using deep learning to support regional water management. *Water Resources Research*, 58(9):e2021WR031910, 2022. doi: <https://doi.org/10.1029/2021WR031910>. URL <https://agupubs.onlinelibrary.wiley.com/doi/abs/10.1029/2021WR031910>.
- N. Žagar. A global perspective of the limits of prediction skill of nwp models. *Tellus A: Dynamic Meteorology and Oceanography*, Jan 2017. doi: 10.1080/16000870.2017.1317573.
- N. Žagar, M. Horvat, Žiga Zaplotnik, and L. M. and. Scale-dependent estimates of the growth of forecast uncertainties in a global prediction system. *Tellus A: Dynamic Meteorology and Oceanography*, 69(1):1287492, 2017. doi: 10.1080/16000870.2017.1287492. URL <https://doi.org/10.1080/16000870.2017.1287492>.

A Long-range spatial error distribution

As shown in Figure 13, the long-range spatial error pattern differs significantly from the 4-day lead time.

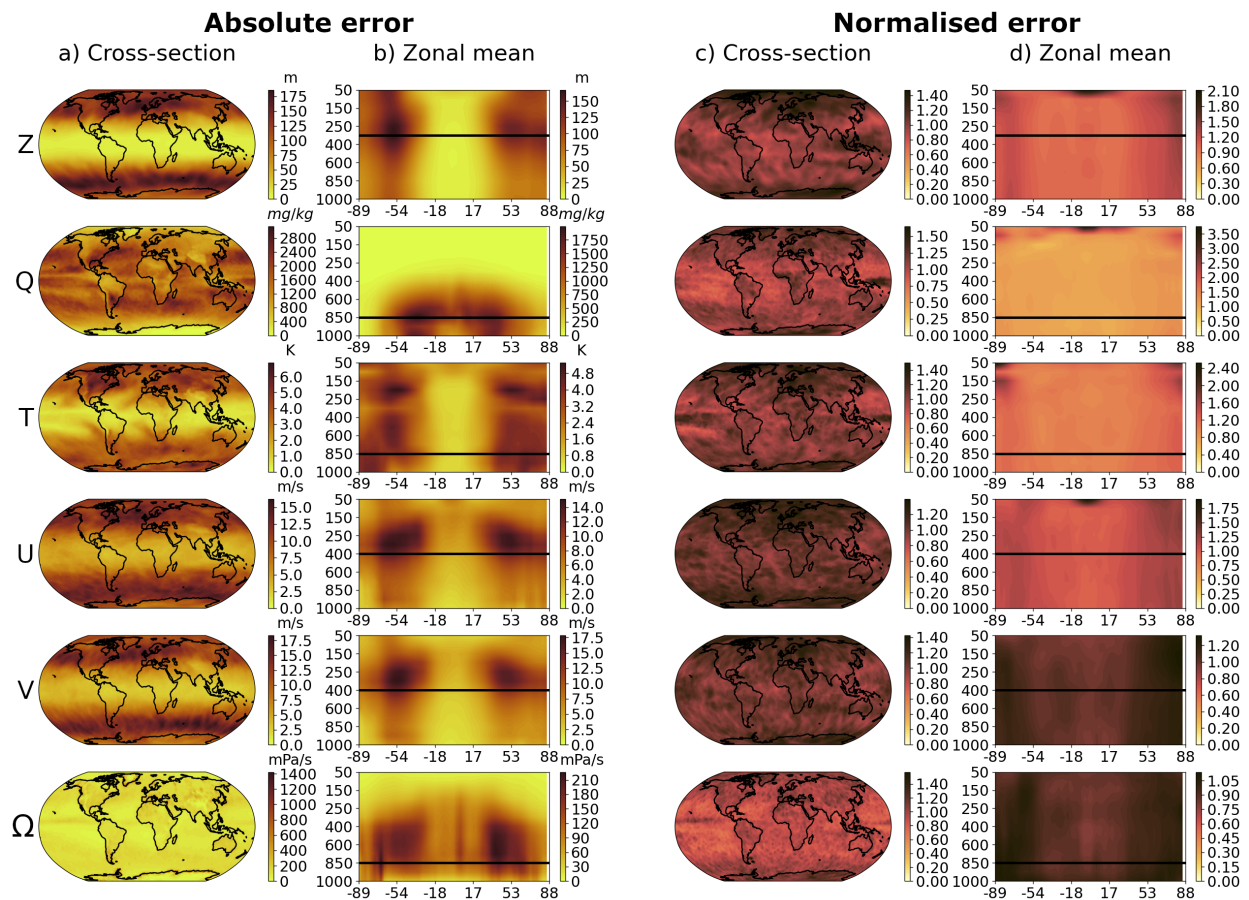


Figure 13: Same as Figure 4, but for 10-day lead time.